

Surface Pile-Up Patterns in Indentation Testing of Cu Single Crystals

S. Kucharski · S. Stupkiewicz · H. Petryk

Received: 19 June 2013 / Accepted: 26 March 2014 / Published online: 15 April 2014
© The Author(s) 2014. This article is published with open access at Springerlink.com

Abstract Nano- and micro-indentation of Cu single crystals is performed in directions not aligned with crystallographic axes. Such tests correspond to mechanical characterization of incidentally oriented grains in a polycrystalline or composite material. Orientation and size dependence of complex patterns of surface piling-up and sinking-in around the imprint are investigated. Experimental observations are compared with finite element simulations based on the large deformation crystal plasticity theory.

Keywords Copper · Nanoindentation · AFM · EBSD · Crystal plasticity · Finite element method

Introduction

Behaviour of materials at different length scales down to nanometer size has recently received increasing attention. Nanoindentation testing is one of the most popular techniques used at present for mechanical characterization of materials at small length scales, not only in terms of hardness and elastic modulus but also in investigations of elastoplastic behaviour of metal single crystals or grains. Interpretation of the results is, however, not a straightforward task, primarily due to the intrinsic anisotropy of both the elastic and plastic responses of a single crystal. Another well-known issue is the dependence of hardness on the indentation depth, extensively investigated recently; cf. [1, 2] for a review.

One of still unresolved problems is the effect of surface piling-up or sinking-in which influence the actual contact area between the indenter and the specimen and affect the hardness

measurement, cf. [3]. This effect is particularly difficult to be accurately described in indentation testing of anisotropic materials like single crystals since the surface topography is then complex and orientation-dependent, also for axisymmetric indenters [4, 5]. On the other hand, complex topography of the surface along with the indentation curve bear information of potential use for local mechanical characterization of anisotropic materials by detailed comparison with the results of numerical three-dimensional (3D) simulations, in particular, with the help of crystal plasticity FEM (finite element method) [4–12].

The aim of this paper is to study anisotropy effects in spherical micro- and nanoindentation of Cu single crystals, in cases when the indentation direction is not aligned with crystallographic axes. Such tests correspond to mechanical characterization of an incidentally oriented grain in a polycrystalline or composite material. An excellent review of the literature on indentation of single crystals has recently been given in [5], therefore, we summarize here only those results of previous works that are most closely related to the present study.

Dyer [13] investigated plastic anisotropy effects in spherical indentation in (001)-oriented Cu single-crystal. Using optical microscopy, he confirmed earlier findings of four hills around the indent at the $\langle 110 \rangle$ azimuths separated by slight depressions at the $\langle 100 \rangle$ azimuths. Referring to the dislocation distribution observed in the vicinity of the imprint, the deformation mechanism of an indented single crystal was described in [13] as a superposition and interaction of slip on two sets of planes. Surface profiles around spherical indents on (100), (110) and (111) surfaces of NiAl single crystal were measured in [14] using a laser scanning microscope. The indents exhibited four-, two- and three-fold symmetry, respectively, with alternate regions of pilling-up and sinking-in similar to those in [13]. Micro-indentation tests on (100), (110) and (111) surfaces of W and Mo single crystals performed in [15] and combined with scanning tunneling

S. Kucharski (✉) · S. Stupkiewicz · H. Petryk
Institute of Fundamental Technological Research, Pawińskiego 5b,
02-106 Warsaw, Poland
e-mail: skuchar@ippt.pan.pl



microscopy indicated that the pile-up formation pattern was still predominantly determined by sample crystallography in spite of using the Vickers indenter.

The analysis of micro- and nanoindentation of copper has been presented in a series of works by Lim et al. [16, 3, 17]. In [16] indentation tests of work-hardened and annealed polycrystalline copper were performed using spherical tips of different radii ($R=7\text{--}1,000\ \mu\text{m}$) and different load forces. The size effect has been observed for smaller radii of tips. It should be noted that the test with smaller indenter radii can be considered to be performed on single crystals, for larger values of radii the stress field induced by indentation comprises more grains. The decrease of nano-hardness with increasing penetration depth has been observed in [3] for polycrystalline copper. The Berkovich and Vickers indenters have been used, and the penetration depth varied from 150 nm to few microns. The residual imprints have been measured using atomic force microscopy (AFM), but the relationship between pile-up patterns and material anisotropy has not been reported.

Wang et al. [4] presented an experimental and numerical study of the dependence of nanoindentation pile-up patterns and microtextures on the crystallographic orientations using copper single crystals. The conical indenter was used in the tests, and the penetration depth was between 10 and 250 nm. Orientation measurements were conducted using a high resolution electron back scatter diffraction (EBSD) technique, and AFM was used to determine the surface topography after indentation. The pile-up patterns obtained experimentally on the surfaces of (001)-, (011)- and (111)-oriented copper single crystals had, according to the authors, four-, two-, six-fold symmetry, respectively, and were well simulated (although not the force-displacement curves) by using the elastic-viscoplastic crystal-plasticity finite element method. In [4] it was observed that all patterns were pile-up rather than sink-in patterns, although the latter might be expected in view of the use of soft copper single crystals with considerable strain hardening. The authors proposed a kinematic explanation in terms of material translation along the intersection vectors of the primary slip systems with the indented surface.

Liu et al. [7] have performed spherical nanoindentation tests on single crystal copper along the [100] direction in combination with 3D FEM simulations performed using an elastic-viscoplastic constitutive model of the crystal. Numerical results showed a four-fold symmetry of the deformation, similar to the AFM image of nanoindentation and consistent with the earlier results mentioned above. The pile-up was more pronounced with smaller indenter radius. FEM simulations indicated that pile-up decreases as the coefficient of friction increases from 0 to 0.4, while the nanoindentation load-displacement relationship remained unaffected. Nanoindentation on single crystal copper were extended in [8] to three crystallographic orientations (100), (011) and (111) of the surface, showing a topographical pattern of pile-

up of four-fold, two-fold, and three-fold symmetry, respectively. No sink-in was observed for the work hardened specimen used. The large deformation FEM simulations of load-displacement relations and the pile-up profiles were found to be in reasonable agreement with experimental observations for all three orientations.

The trend of using 3D FEM analysis to promote understanding of indentation into anisotropic crystals is being continued in the literature. The spherical indentation in the single crystals of copper and zinc was simulated in [9] by using rate-dependent crystal plasticity in a large deformations FEM code. It has been observed that the plastic zone preferentially grows along the slip system directions. Anisotropic pile-up or sink-in patterns have been analysed. A rate-independent crystal plasticity model was used in [11] to simulate the above-mentioned experimental indentation results given in [7, 8]. The influence of a pyramidal indenter symmetry and crystal symmetry on pile-up patterns generated in the micro-indentation tests of fcc single crystal of Ni-base superalloy (CMSX-4) were studied experimentally and theoretically in [12]. It has been observed at some distance from contact boundary that the direction of pile-up depends on crystallographic orientation rather than on azimuthal indenter orientation. The author concludes that in the case of fcc crystal the pile-up pattern is mainly governed by the geometry of the slip systems.

A systematic study of pile-up patterns in indentation in TiAl has been presented by Zambaldi and Raabe [5]. In spite of another material tested, the approach and results given there constitute a useful basis for the present work. In the paper, the nanoindentation test with Berkovich and sphero-conical tips were performed experimentally and modeled using crystal plasticity FEM with account for twinning systems. The residual imprint topography was measured using AFM. The indentation tests were performed in different crystallographic directions with the maximal penetration depth of about 300 nm. In a number of systematic numerical investigations based on the parameters identified, the correlation of the pile-up pattern and crystal orientation throughout the basic unit triangle was determined. It was shown that characterization of the orientation-dependent pile-up behavior by the combined use of experimental and computational methods introduces a number of useful analytical tools. Axisymmetric indenters are particularly suited for that approach.

Density of dislocations in the plastic zones generated in nanoindentation tests of single crystals has been analysed in [18, 19] using transmission electron microscopy (TEM). The authors have observed that despite of sharp triangular tip (Berkovich), the densely dislocated zone had a circular shape for low loads while for larger loads followed the crystallographic direction of slip systems. Core and a surrounding low dislocation density zone did not evolve in a self similar manner with increasing load. Significant relaxation of the dense dislocation structure at small penetration depths has

been observed. Model of expansion of dense dislocation zone was used to modify the formulae for prediction of increase of hardness due to decreasing penetration depth.

In spite of the above-mentioned valuable contributions, there are still open questions concerning consistent modeling of indentation test in anisotropic media in nano- and micro-scale. It is difficult to find in a single paper a complete comparison of numerical and experimental results for all the quantities observed in the instrumented indentation test, i.e. load-penetration (F - h) relation and pile-up or sink-in profiles. Some authors focus on F - h curves, other analyze the shape of residual imprints obtained in experiment and in numerical simulations. When sphero-conical tips are used then it is not always clear whether only the spherical or both conical and spherical parts influence the deformation pattern. Finally, the size effect on pile-up and sink-in profiles is not yet clear. Further development of the methods of identification of parameters of anisotropic metal crystals by nanoindentation is thus still a challenging task.

In this work, we perform a detailed study of micro- and nano-indentation tests in the direction not fully explored in the literature. First, the study is focused on anisotropy effects at spherical indentation in Cu single crystals in two directions not aligned with crystallographic axes, which goes beyond more typical experimental data obtained for three special crystallographic directions. Second, the measurements of orientation and size dependence of complex patterns of surface piling-up and sinking-in around the imprints are provided simultaneously with load-penetration curves for the same tests, which enhances the database for validation of crystal plasticity models and is frequently missing in the literature. Third, numerical simulations of the indentation tests are performed and compared to the experimental measurements of both the surface geometry and load-penetration relationship for indentation in non-crystallographic directions. For those purposes, the topography of residual imprints was measured using AFM in the nano-scale, and high resolution scanning profilometer in the micro-scale. Numerical simulations of the tests have been performed using a large-deformation crystal plasticity constitutive law implemented in a FEM code, with due account for the crystal orientation. The final aim has been to check how far the scale-independent crystal plasticity law is able to provide detailed description and prediction of the load-penetration curves and out-of-plane patterns of surface topography around the indents in micro- and nano-scales.

Experimental

Experimental Setup and Sample Preparation

The CSM Open Platform equipment used to perform indentation tests is described briefly. The micro-indenter MHT was

applied in micro-scale and ultra-nano indenter UNHT was used in nano-scale to measure load-penetration curves of single crystal copper. In the nano-system, the maximum penetration depth is $h=50\ \mu\text{m}$ and load range is $F=0\text{--}50\ \text{mN}$ (standard range). The displacement resolution and load resolution are $0.0005\ \text{nm}$ and $2.5\ \text{nN}$, respectively. The thermal drift equals $0.5\ \text{nm}/\text{min}$. Spherical diamond indenter with radius $5\ \mu\text{m}$ was used. This value of tip radius has been confirmed in purely elastic indentation test in fused silica where the Hertz equation has been fulfilled. In the microindentation test, the displacement resolution and load resolution are $0.3\ \text{nm}$ and $100\ \mu\text{N}$, respectively, and tip radius is $200\ \mu\text{m}$. The residual imprints generated in the nanoindentation tests were scanned using the atomic force microscope Bruker AFM Nanos integrated in the CSM device. To scan imprints in the microscale, the scanning profilometer (Hommel-Etamic T8000 Nanoscan), vertical resolution less than $1\ \text{nm}$, has been used independently.

A high purity (99.9999 %) copper bars have been manufactured in a slow crystallization process and as a result a multi-crystalline material with large grains (grain size about $10\ \text{mm}$) has been produced. The material has been expected to exhibit considerable work hardening. Next, the bars were cut into samples using electrical discharge machining (spark erosion). Each specimen was polished to produce mirror-reflecting surfaces for indentation tests. The polishing processes were performed by using grinding papers of 1,000, 1,500, 2,000 and 2,500 grits. The diamond suspension has not been used as the small particles could be pressed in the soft copper. In the mechanical polishing the layer of thickness of about $400\ \mu\text{m}$ has been removed, to annihilate possible traces of the electrical discharge. After the mechanical polishing, the electro-polishing was applied in several steps. After each step the nanoindentation test was performed and the resulting load-penetration curves were compared. The electro-polishing process has been finished when the P-h curves measured after two consecutive steps were the same. The surface roughness was about $15\ \text{nm}$.

In the indentation tests in the nano-scale, four load levels were applied: 6, 10, 16, 20 mN that were executed at different location to verify repeatability of the tests. It has been observed that the variation of loading rates in range $6\text{--}18\ \text{mN/s}$ does not influence the load-penetration curves. Finally, the loading rate $16\ \text{mN/s}$ was applied and hold time was $2\ \text{s}$.

At the micro-level the load was $8\ \text{N}$ and $11.8\ \text{N}$ and the loading rate was $10\ \text{N}/\text{min}$ with hold time $2\ \text{s}$. The distance between indents was about 5–6 times greater than the diameter of residual imprint. After the tests, the residual imprints were scanned to obtain a topography of pile-up and sink-in. All tests were performed in room temperature. Generally, the performed tests exhibited a good reproducibility, however some tests that extremely drifted away from mean results were not taken into account. As in the applied instrument (CSM)

Table 1 Euler angles of the investigated crystals

	ϕ	θ	ψ
C1	36	12	316
C2	326	42	33

the top surface referencing technique is used, i.e. a differential measurement between the sample surface and the indentation depth is conducted, the mode of samples clamping does not influence the indentation results.

In the present study, two crystals (large grains) of different crystal orientations, denoted as C1 and C2 have been investigated. The crystals orientations have been specified by using the scanning electron microscope Auriga-type (Zeiss) and the EBSD (electron backscatter diffraction) method. The Euler angles are shown in Table 1 and the pole figures of $\{100\}$ and $\{111\}$ axes for both crystals are presented in Fig. 1.

Indentation Tests

The load-penetration curves in the nanoindentation test are presented in Fig. 2, where two crystals C1 and C2 indented at different peak loads are compared.

A good repeatability of the tests can be observed and a small scatter of results is seen for different loads. In spite of different crystal orientations, Fig. 2 shows negligible difference between the responses of crystals C1 and C2. At the beginning of the loading curves, for the loads less than 0.8 mN in the case of crystal C1 and less than 2 mN in the case of crystal C2 one can observe the known pop-in effect: an initial part of the curve corresponds to the purely elastic material behaviour and after a jump it is continued according to an elastic–plastic behaviour. This effect is more evident for the crystal C2.

The microindentation tests (nominal tip radius $R=200\ \mu\text{m}$) have been performed for two maximal loads $F=8\ \text{N}$ and $F=11.8\ \text{N}$, the latter corresponds approximately to the same ratio h/R as in the case of 16 mN load in nano-scale. The results are presented in Fig. 3. As in the nano-scale, the load-penetration curves for crystals C1 and C2 are practically the

same, the difference between F - h curves for different crystals being not greater than the scatter of results. Analogous observation has been reported in [17], where the differently oriented copper crystals exhibited similar Brinell hardness in micro-scale (for tip radius $R=200\ \mu\text{m}$).

Figure 4 shows the normalized load-penetration curves of crystal C1. The penetration h is normalized by the corresponding radius R and the indentation force F is normalized by R^2 . The difference in the normalized load-penetration curves corresponding to micro- and nanoindentation indicates a significant size effect. One can conclude that for similar deformation range, characterized by a similar ratio h/R , the material exhibits larger stiffness (hardness) in the nano-scale than in the micro-scale. This familiar size-effect, known as “smaller is stronger”, has not always been observed [8]. The difference between the F - h curves corresponding to different crystals is here small and is similar in the nano- and micro- scale.

Surface Topography

As the spherical indenter tip exhibits axial-symmetry, deviation of residual imprint from the axi-symmetrical shape is basically a result of material anisotropy, with perturbations due to surface roughness, material nonuniformity, etc. The influence of anisotropy on the shape of residual imprints is readily visible in the micro-scale. The optical microscope images and profilometry maps for microindentation performed in the crystal C1 are presented in Figs. 5 and 6.

Spherical indentation in the crystal C1 resulted in a quasi-rectangular shape of the projection of residual imprint visible in optical microscope. The observed shape is a geometric result of an alternate pattern of smaller pile-up and more pronounced sink-in of the free surface just around the contact, which will be more clearly seen later in Fig. 13(a). Similar observations were reported by Dyer [13] for spherical indentation ($2R=6.35\ \text{mm}$) of Cu single crystal in $[100]$ direction. Near the corners of the residual imprint, on the hillocks, traces of slip planes can be observed as shown in Fig. 5. The deviation from precise

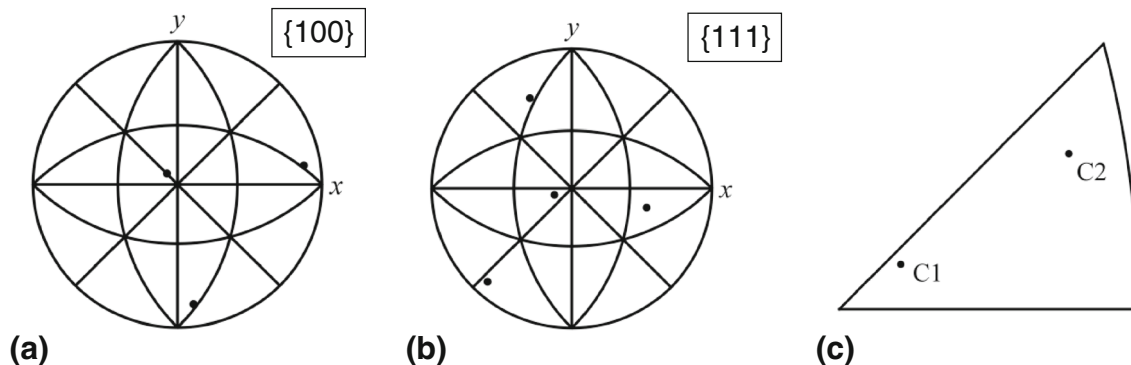


Fig. 1 Pole figures of analysed copper crystals: (a) C1; (b) C2; (c) inverse pole figure

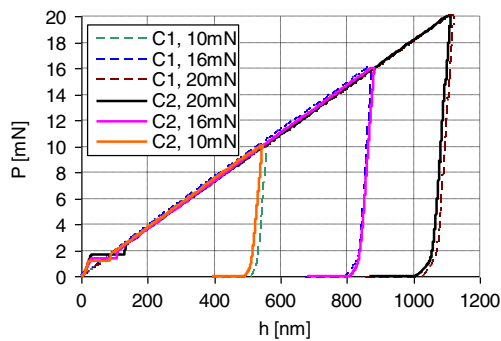


Fig. 2 Load-penetration curves for single crystals indented with different forces in nano-scale: comparison of C1 and C2

symmetry of the imprints can be attributed to deviation of the indentation direction from a high symmetry axis of the crystal, and to a certain extent to initial waviness of the surface. The residual imprints are qualitatively similar for different values of load (8, 11.8 N). The orientation of pile-up patterns corresponds to the symmetry of primary slip systems.

In the case of the crystal C2, Figs. 7 and 8, the shape of projection of the residual imprint is closer to axi-symmetric one due to the fact that the pile-up and particularly the sink-in are less evident than in the crystal C1. This can be seen when the profiles of residual imprints for directions marked in Figs. 5 and 7 are compared. In C2 a different pattern of pile-up than in C1 is observed, namely, closer to a two-fold symmetry than to a four-fold one. Note that the two-fold symmetry for the indentation direction [011] was found in earlier papers, e.g. [4].

Representative AFM measurements of the imprints in nanoscale are presented in Figs. 9 and 10 for the crystals C1 and C2, respectively. The zero height level refers to the specimen surface before indentation. In the case of crystal C1 one can observe a narrow, quasi-rectangular zone of sink-in close to the indent (around the contact boundary) and next, more distant from the contact boundary, the pile-up hillocks occur. The narrow sink-in zones around the indent have rather oval shape in the case of crystal C2, which can be seen in Fig. 10. The pile-up zone in turn is not axisymmetric and is composed of some hillocks.

It has been observed that the system of pile-up and sink-in around the contact zone depends on load level and is less

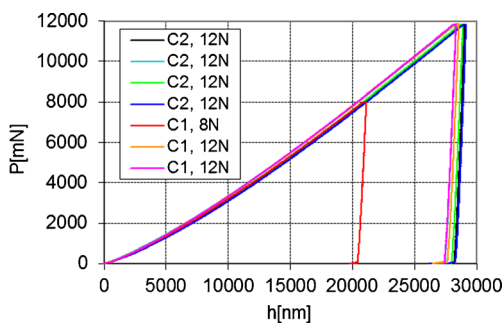


Fig. 3 Load-penetration curves for different crystals in micro-scale

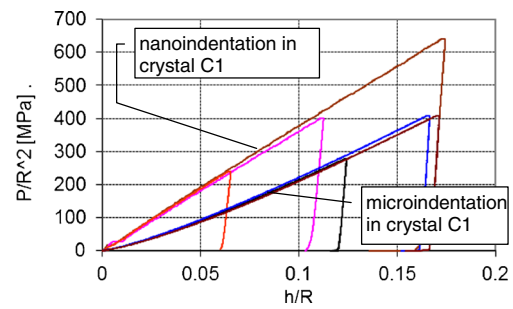


Fig. 4 Comparison of normalized load-penetration curves specified in micro- and nano-scale

regular than in the case of microindentation. From analysis of numerous nanoindentation experiments performed with $5 \mu\text{m}$ tip and for different loads (results are not presented here due to limited space) one can conclude that for the same value of load and for fixed crystal orientation the pile-up pattern is more or less qualitatively repeatable.

The pile-up pattern depends on both the crystal orientation and applied load. This observation matches up with the results presented in [18], where the shape of dense dislocation region generated in nanoindentation test depended on the applied load.

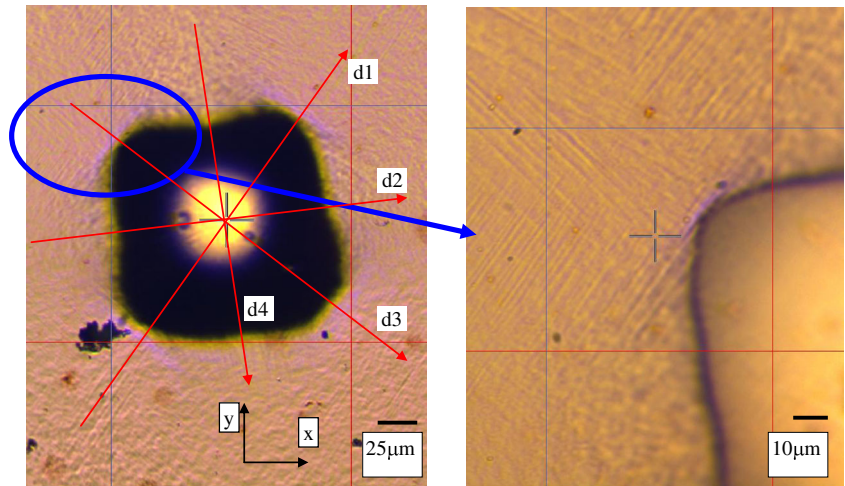
The deformation mechanisms of single crystals in nano-scale have been investigated extensively in the literature on the basis of micropillars compression tests and nanoindentation tests, which were simulated using both crystal plasticity and molecular dynamics approaches. It has been concluded that the value of flow stress can be associated with the emission of new dislocations from small immobile defects inside the material that contribute to the size dependence of strength in nanoscale [20]. In [21] the authors suggested that at small size scales, for materials where dislocation density is limited, the deformation mechanisms can be dominated by dislocation nucleation. One can expect that in the nano-scale the response of material depends on both dislocation nucleation at defects and dislocation propagation on slip planes. An indirect confirmation of the above observations can be found in the paper [22] where the homogeneous dislocation nucleation in the nanoindentation test in free-of-defects single crystal has been studied using static atomic simulation. It has been shown that in such a crystal the indentation size effect is very weak.

For the same ratio h/R , which can be considered as a measure of deformation beneath the indenter, the pile-up and sink-in pattern generated in micro-scale ($F = 11.8 \text{ N}$) is somewhat different from that in the nano-scale ($F = 16 \text{ mN}$), as shown in Fig. 11.

Crystal Plasticity Model and Finite Element Modelling

The well-known constitutive framework of crystal plasticity [23, 24] is used to model elastic–plastic deformations of single crystals at finite strain. The basic relationships of the

Fig. 5 Optical microscope images of residual imprint in crystal C1, $F=8$ N (microindentation)



formulation adopted in this work are provided below; the details can be found, for instance, in [23, 24].

Multiplicative decomposition of the deformation gradient \mathbf{F} into lattice deformation part \mathbf{F}^e (stretch and rotation) and plastic part \mathbf{F}^p yields

$$\mathbf{F} = \mathbf{F}^e \mathbf{F}^p, \quad \mathbf{C}^e = \mathbf{F}^{eT} \mathbf{F}^e, \quad \mathbf{L}^p = \dot{\mathbf{F}}^p \mathbf{F}^{p-1}, \quad (1)$$

where \mathbf{C}^e is the elastic Cauchy-Green tensor and \mathbf{L}^p is the plastic velocity gradient, both defined in a locally unstressed, intermediate configuration of constant lattice orientation.

Anisotropic elastic response of the crystal is taken to be governed by the St. Venant-Kirchhoff model in the form

$$\mathbf{S}^e = \mathbf{L} \mathbf{E}^e, \quad \mathbf{E}^e = \frac{1}{2} (\mathbf{C}^e - \mathbf{1}), \quad (2)$$

where \mathbf{S}^e is the second Piola-Kirchhoff stress tensor relative to the intermediate configuration, and \mathbf{L} is a positive-definite, fourth-order tensor of elastic moduli. In the present case of cubic symmetry, \mathbf{L} is expressed in terms of three elastic constants C_{11} , C_{12} and C_{44} .

Rate-independent anisotropic plastic response is governed by the Schmid law, taken here in the regularized form [24, 25]. A single smooth yield condition is introduced for all slip systems,

$$F(\boldsymbol{\tau}, \tau_s^c) = \left(\sum_{s=1}^{N_s} \left(\frac{\tau_s}{\tau_s^c} \right)^{2n} \right)^{1/(2n)} - 1 \leq 0, \quad (3)$$

which approximates the yield conditions for individual slip systems at sufficiently high exponent n . In equation (3), τ_s^c denotes the critical resolved shear stress (CRSS) on slip sys-

Fig. 6 Scanned residual imprints in crystal C1: (a) $F=8$ N (microindentation)

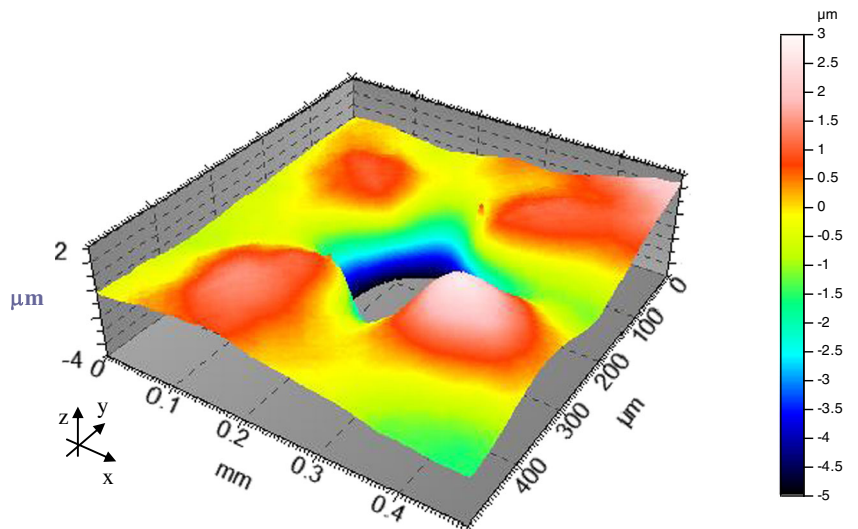
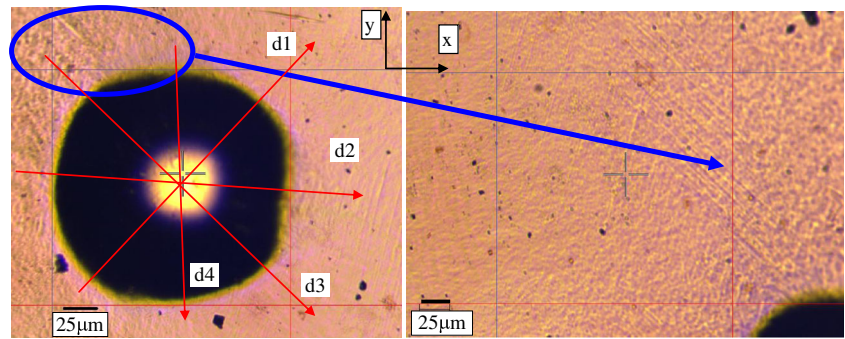


Fig. 7 Optical microscope images of residual imprint in crystal C2 ($F=11.8$ N, microindentation)



tem s , and τ_s is the actual resolved shear stress on slip system s defined in terms of the Mandel stress tensor \mathbf{M} or the Kirchhoff stress tensor $\boldsymbol{\tau}$ as follows:

$$\tau_s = \mathbf{M} \cdot (\mathbf{s}_s \otimes \mathbf{n}_s), \quad \mathbf{M} = \mathbf{C}^e \mathbf{S}^e = \mathbf{F}^{eT} \boldsymbol{\tau} \mathbf{F}^{e-T}, \quad (4)$$

where unit vectors \mathbf{n}_s and \mathbf{s}_s define, respectively, the slip-plane normal and slip direction for slip system s in the intermediate configuration. Plastic deformation is governed by a rate-independent associated flow rule,

$$\mathbf{L}^p = \dot{\lambda} \frac{\partial F}{\partial \mathbf{M}} = \sum_{s=1}^{N_s} \dot{\gamma}_s \mathbf{s}_s \otimes \mathbf{n}_s, \quad \dot{\lambda} \geq 0, \quad \dot{\lambda} F = 0, \quad (5)$$

and it can be shown that the specific form (3) of the yield condition indeed describes plastic deformation by crystallographic slip on individual slip systems, as indicated in equation (5). The above regularization is similar, but not identical,

to the popular viscous regularization which results in a rate-dependent plastic response, cf. e.g. [24].

Hardening of individual slip systems is governed by the following evolution equation:

$$\dot{\tau}_s^c = \hat{\theta} \sum_{r=1}^{N_s} q_{sr} \dot{\gamma}_r, \quad (6)$$

where $q_{rs}=1$ for coplanar slip systems (self hardening) and $q_{rs}=q>1$ for non-coplanar systems (latent hardening). The instantaneous hardening modulus $\hat{\theta}$ is defined by a Voce-like hardening law [26],

$$\hat{\theta} = \frac{d\hat{\tau}}{d\Gamma}, \quad \hat{\tau} = \hat{\tau}_0 + (\hat{\tau}_1 + \hat{\theta}_1 \Gamma) \left(1 - \exp\left(-\hat{\theta}_0 \Gamma / \hat{\tau}_1\right) \right), \quad \hat{\Gamma} = \sum_{s=1}^{N_s} |\dot{\gamma}_s|, \quad (7)$$

where $\hat{\tau}_0$ and $\hat{\tau}_0 + \hat{\tau}_1$ are, respectively, the initial and the back-extrapolated CRSS, while $\hat{\theta}_0$ and $\hat{\theta}_0 + \hat{\theta}_1$ are, respectively, the initial and the asymptotic hardening rate.

Fig. 8 Scanned residual imprint in crystal C2 for $F=11.8$ N (microindentation)

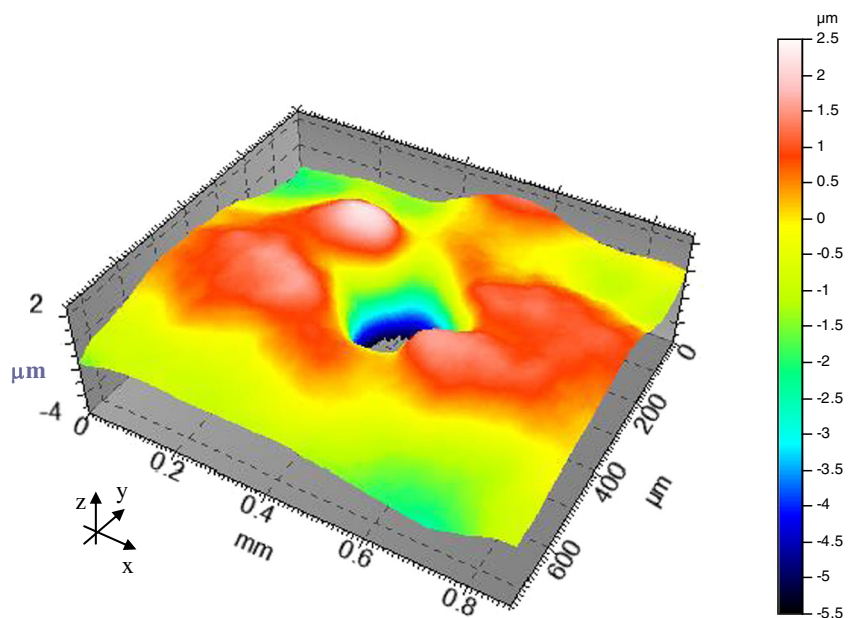
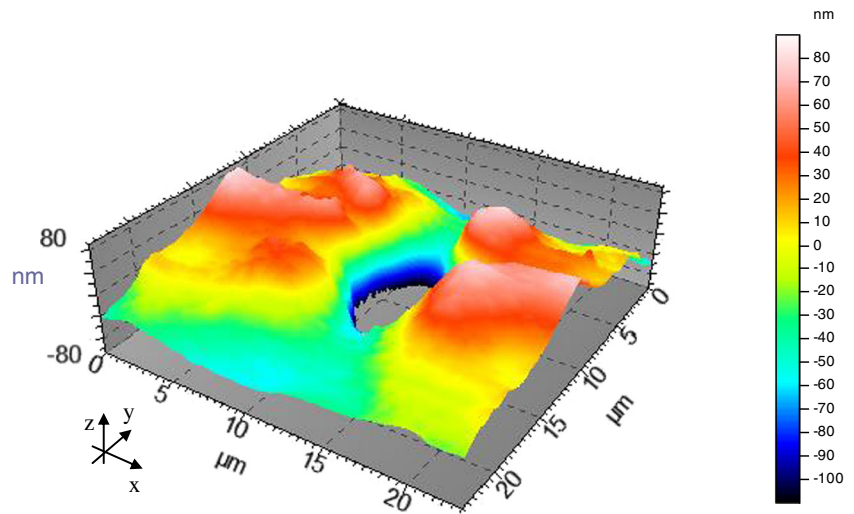


Fig. 9 Residual imprints in crystal C1 (nanoindentation) for $F=20$ mN



The above crystal-plasticity model has been implemented in a large-strain displacement-based finite element code. The implicit backward-Euler integration scheme is applied to arrive at incremental constitutive equations, and an exponential map integrator is used to consistently treat plastic incompressibility, cf. [27], thus resulting in the following update of the plastic part of deformation gradient:

$$\mathbf{F}_{k+1}^p = \exp\left(\sum_{s=1}^{N_s} \Delta\gamma_s \mathbf{s}_s \otimes \mathbf{n}_s\right) \mathbf{F}_k^p. \quad (8)$$

In order to avoid volumetric locking effects, the F-bar element [28] has been used in the computations. The indenter has been assumed rigid, and frictionless contact constraints have been enforced using the augmented Lagrangian method [29]. Implementation and computations have been performed

using the *AceGen/AceFEM* system (<http://www.fgg.uni-lj.si/Symech/>), see [30, 31] for the details of automation of the solid and contact formulations.

Finite element simulations have been carried out for the micro-indentation test with the indenter radius $R=200$ μm . The finite element mesh has dimensions $1,200 \times 1,200 \times 600$ μm . The mesh has been significantly refined in the central part of the dimensions $300 \times 300 \times 100$ μm . The mesh consists of 22,944 eight-node solid elements, and the total number of degrees of freedom is 73,083 including the contact Lagrange multipliers.

Model parameters used in the computations reported in this work are provided in Table 2. Typical elastic constants are taken from the literature. For the latent hardening ratio, a typical value of $q=1.4$ has been adopted. A reasonably high value of the exponent $n=20$ has been used. Finally, the initial CRSS and hardening parameters have been identified such that the load-penetration curve of crystal C1 in micro-

Fig. 10 Residual imprints in crystal C2 (nanoindentation) for $F=20$ mN

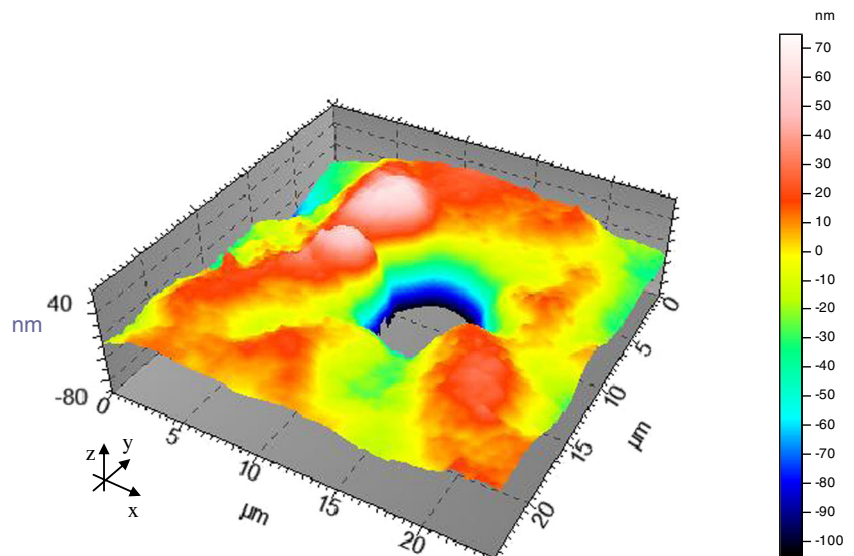
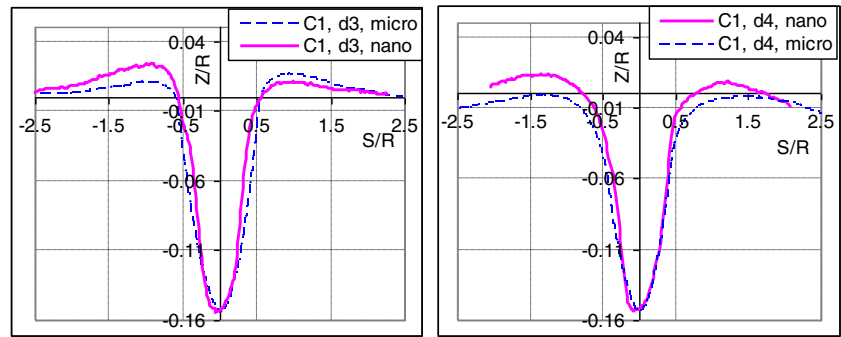


Fig. 11 Comparison of residual imprints profiles obtained in nano- and micro-scale in crystal C1 for directions d3 and d4



indentation is reproduced with good accuracy, see below. The load-penetration curve for crystal C2 and deformation patterns for any orientation are predicted based on this identification. Note, however, that the hardening parameters cannot be uniquely determined from the indentation curve.

Comparison of the Numerical and Experimental Results

The numerical model described above has been applied to simulate the microindentation tests. Consideration of the size effects observed at the nanoscale, cf. Fig. 4, would require an extension of the model, for instance by including the strain gradient effects, which is beyond the scope of this paper. The results of computations are thus presented in comparison to the experimental observations at the micro-scale only. The load-penetration curves are presented in Fig. 12(a) and (b) for the crystals C1 and C2, respectively.

In the case of crystal C1 a very good agreement of numerical and experimental results has been obtained for the parameters fit as described above. For the crystal C2, the loading part of the predicted load-penetration curve is somewhat stiffer than that for the crystal C1, and hence than that measured experimentally for both crystals with negligible scatter. A possible explanation can be conjectured from slip-line patterns in Figs. 5 and 7. They indicate a deformation split into single-slip domains, which can be energetically preferable to simultaneous activity of multiple slip-systems, cf. e.g. [32, 33]. The elastic–plastic FE model used here does not involve incremental energy minimization and may not reproduce correctly such deformation splitting.

The comparison of topography of predicted numerically and experimental residual imprints is presented in Figs. 13, 14 and

15. Marks x, y denote the coordinate system with respect to which the Euler angles presented in Table 1 have been specified. In the crystal C1 the sequence of four alternate hillocks and depressions occurs around the imprint, Fig. 13(a), which results in a rectangular shape of the projection of the contact boundary presented in the photo of the imprint in Fig. 5. Qualitatively and quantitatively similar topography has been obtained in the numerical simulation, Fig. 13(b).

For the crystal C1, a more exact quantitative comparison of the pile-up and sink-in heights is shown in Fig. 14 where the profiles in d3 and d2 directions marked in Fig. 5 are presented. One can observe that the sink-in predicted in numerical solution and obtained experimentally are similar, while the pile-up hillocks are slightly higher and closer to the contact boundary in the numerical solution. Nevertheless, the accuracy of FEM predictions of surface topography in the vicinity of the imprint may be regarded as satisfactory.

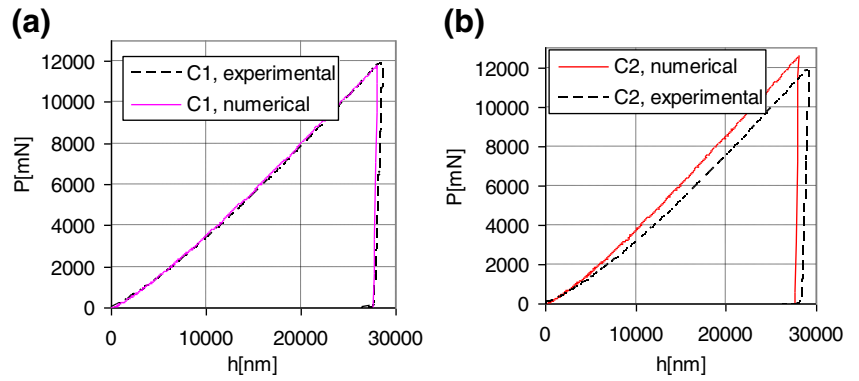
For the crystal C2 one observes a qualitative agreement of the numerically and experimentally obtained pile-up patterns, cf. Fig. 15, however, the hillocks are more distinct in the case of numerical solution in Fig. 15(b). In the experiment, pile up hillocks are separated only by a very shallow valley, cf. Figs. 8 and 15(a). As in the case of crystal C1, the pile-up height predicted in the numerical simulations is somewhat greater than that observed in the experiment.

Analogous analysis of imprints topography in the nano-scale can be presented on the base of maps shown in Figs. 9 and 10. In the case of crystal C1, Fig. 9, they are qualitatively similar to those in the micro-scale, although the pile-up pattern is less pronounced and sink-in pattern is more pronounced than in the micro-scale. It is essential that the directions of the sink-in are the same in nano- and micro-scale, thus the characteristic directions of the imprint topography do not depend on the load and are uniquely related to the crystal orientation. Correlation between the location of pile-up and the orientation

Table 2 Parameters of the crystal plasticity model

C_{11}	C_{12}	C_{44}	$\hat{\tau}_0$	$\hat{\tau}_1$	$\hat{\theta}_0$	$\hat{\theta}_1$	q	n
170 GPa	124 GPa	75 GPa	12 MPa	54 MPa	180 MPa	6 MPa	1.4	20

Fig. 12 Comparison of experimental and numerical load-penetration curves in micro-scale: (a) crystal C1, (b) crystal C2



of the indented crystal is here more complex than in the case of indentation in a direction aligned with a symmetry axis of a crystal.

For the crystal C2, Fig. 10, the similarity of residual imprints in nano- and micro-scale can be found only for the larger value of load, i.e. 20 mN in the nano-scale, where a

weak outline of the pile-up pattern that exhibits twofold symmetry, similarly as in the micro scale, is visible. In contrast to the indentation in micro-scale, the characteristic directions of this imprint are difficult to recognize.

In the literature, attention was usually focused on indentation in directions aligned with a symmetry axis of a crystal.

Fig. 13 Residual imprints in crystal C1 for $F=11.8$ N (micro-scale): (a) experimental (b) numerical simulation

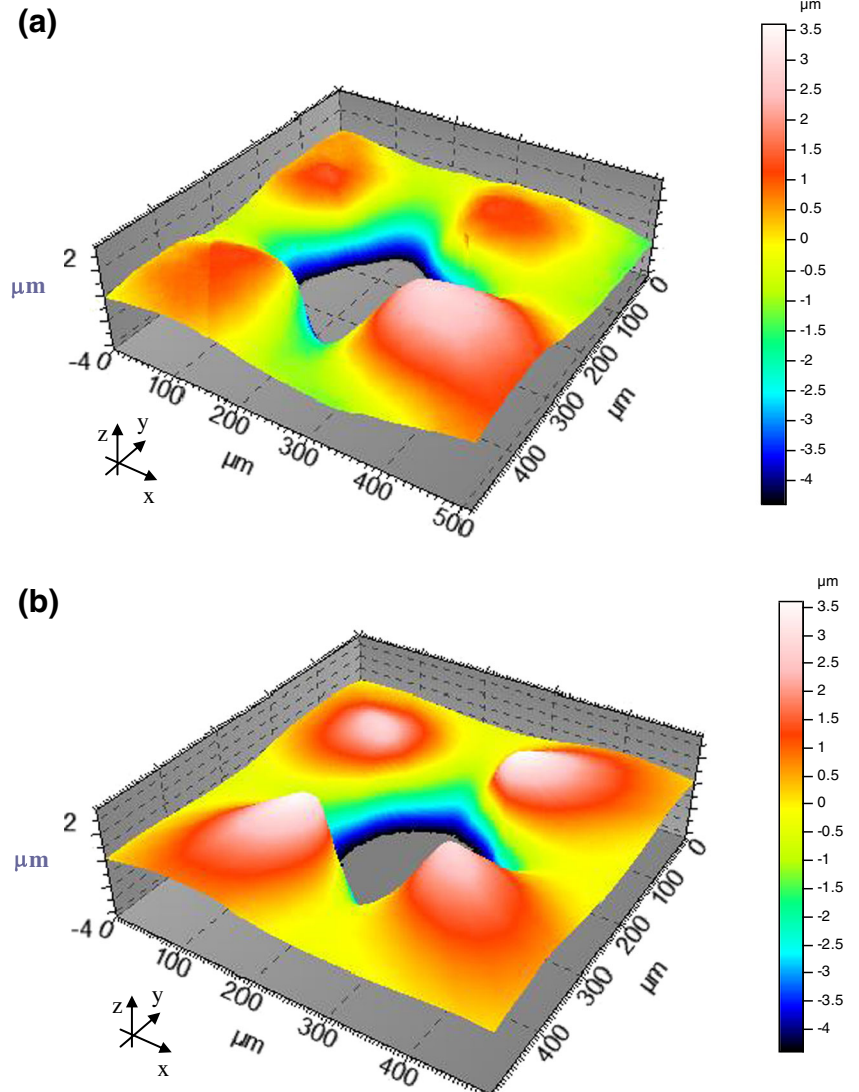
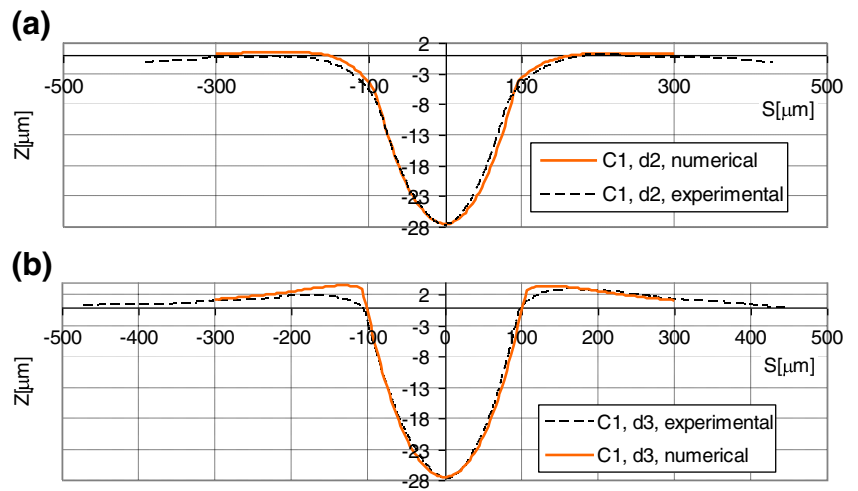


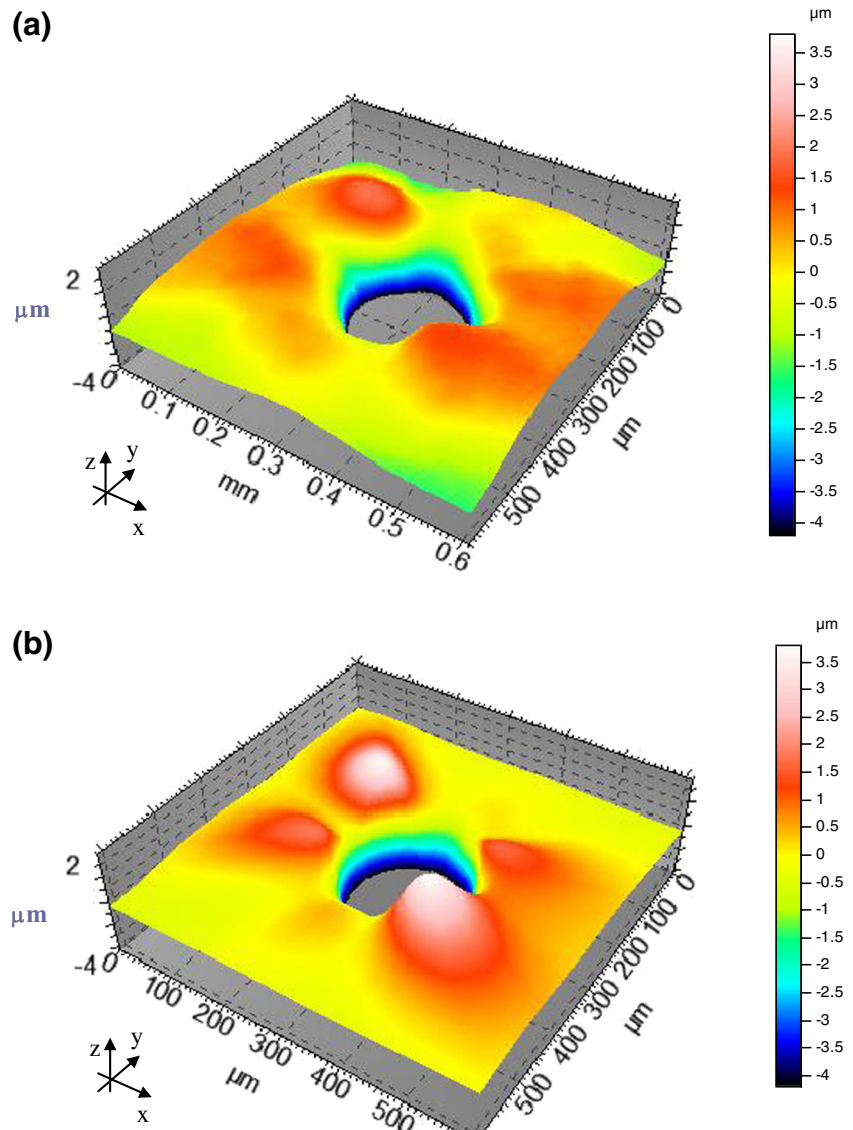
Fig. 14 Comparison of simulated and experimental profiles for directions d1, d3 for crystal C1



For a copper single crystal, it has been observed [4] that the profile around the indent on the (001)-oriented crystal reveals

four-fold symmetry, for the (011)-oriented crystal two-fold symmetry, and for the (111)-oriented crystal six-fold

Fig. 15 Residual imprints in crystal C2 for $F=11.8$ N (micro-scale): (a) experimental (b) numerical solution



symmetry (actually, a three-fold symmetry is expected for the (111)-oriented crystal). The former correlation is found also in the present case of crystal C1 where there is a small inclination of the crystal (001) axis with respect to the indentation direction z perpendicular to surface of the sample. This inclination is represented by the second Euler angle, $\theta=12^\circ$. The experimental pile-up pattern exhibits here approximately a four-fold symmetry and is rotated in accord with the remaining Euler angles ψ, ϕ , cf. Table 1.

The correlation is more complex in the case of crystal C2, where the angle between the [001] crystal axis and z axis equals 42° . The symmetry of pile-up pattern is less clear and closer to two-fold one, however, it would be difficult to specify other Euler angles on the base of analysis of pile-up hillocks directions. Although the indentation direction for this sample is closer to (111), three-fold symmetry is not yet observed here.

Conclusions

Dependence of the imprint topography on the orientation of an indented crystal has been found considerably more significant than a practically negligible difference between measured indentation curves for two copper single crystals of distinct orientations, denoted as C1 and C2. Hence, detailed measurements of surface piling-up and sinking-in around the indent can provide more useful information on anisotropic behaviour of metal single crystals than load-penetration curves alone. On the other hand, size dependence of the scaled indentation curves (and hardness) corresponding to tip radii of 5 and 200 μm and indentation force 6–20 mN and 8–11.8 N, respectively, is found substantial. This has confirmed the size-effect in metal single crystals in the nano-scale, which obviously cannot be modeled by the standard size-independent models of crystal plasticity.

The size-dependence of the surface topography around the indent is more complicated. It has been observed, similarly as in [13, 14], that not only pile-up but also sink-in occurs around the imprint in the indentation test of single crystal copper. Additionally, this is found to be more evident in the case of micro-scale than in nano-scale. For the two crystals tested, the surface topography around an indentation imprint exhibits four consecutive sectors of pile-up and of sink-in, except the less clear nanoindentation pictures for the crystal C2. For crystal C1 the directions of the sink-in are the same in the nano- and micro-scale, thus the characteristic directions of the imprint topography do not depend on the load and are uniquely related to the crystal orientation. However, a quantitative comparison of imprints generated at the micro- and nano-scale shows that the nano-pile-up pattern cannot be obtained by a simple scaling of the micro-pattern. Moreover, scaling procedure is not sufficient to make a transition between different

imprints that correspond to different loads at the nano-scale. One can conclude that in spite of the use of a “blunt” spherical indenter, different deformation mechanisms occur for different loads and for different scales.

Unlike in earlier studies, detailed quantitative comparison of experimental and numerical results concerning both the load-penetration curves and surface topography around the indents has been performed for micro- and nano-indentation in two directions not aligned with the high-symmetry axes of a Cu crystal. The accuracy of crystal plasticity FEM predictions of the complex pile-up and sink-in pattern for indentation in such directions can be regarded as satisfactory in the micro-scale. In the nano-scale the agreement is less clear. It remains an open question whether the difference is due to a size-dependent deformation pattern beneath the indenter or, for instance, due to the roughness of the real crystal surface, inadequate surface preparation or inaccurate indenter geometry.

Acknowledgments The present research was partially supported by the Polish National Science Centre, grant NN 501 0672 40

Open Access This article is distributed under the terms of the Creative Commons Attribution License which permits any use, distribution, and reproduction in any medium, provided the original author(s) and the source are credited.

References

1. Fischer-Cripps A (2006) Critical review of analysis and interpretation of nanoindentation test data. *Surf Coat Technol* 200:4153–4165
2. Pharr GM, Herbert EG, Gao Y (2010) The indentation size effect: a critical examination of experimental observations and mechanistic interpretations. *Annu Rev Mater Res* 40:271–292
3. Lim YY, Chaudri MM (1999) The effect of the indenter load on the nanohardness of ductile metals: an experimental study on polycrystalline work-hardened and annealed oxygen-free copper. *Philos Mag A* 79:2979–3000
4. Wang Y, Raabe D, Klueber C, Roters F (2004) Orientation dependence of nanoindentation pile-up patterns and of nanoindentation microtextures in copper single crystals. *Acta Mater* 52:2229–2238
5. Zambaldi C, Raabe D (2010) Plastic anisotropy of c-TiAl revealed by axisymmetric indentation. *Acta Mater* 58:3516–3530
6. Fivel MC, Robertson CF, Canova GR, Boulanger L (1998) Three-dimensional modeling of indent-induced plastic zone at a mesoscale. *Acta Mater* 46:6183–6194
7. Liu Y, Wang B, Yoshino M, Roy S, Lu H, Komanduri R (2005) Combined numerical simulation and nanoindentation for determining mechanical properties of single crystal copper at mesoscale. *J Mech Phys Solids* 53:2718–2741
8. Liu Y, Varghese S, Ma J, Yoshino M, Lu H, Komanduri R (2008) Orientation effects in nanoindentation of single crystal copper. *Int J Plast* 24:1990–2015
9. Casals O, Forest S (2009) Finite element crystal plasticity analysis of spherical indentation in bulk single crystals and coatings. *Comput Mater Sci* 45:774–782



10. Lee WB, Chen YP (2010) Simulation of micro-indentation hardness of FCC single crystals by mechanism-based strain gradient crystal plasticity. *Int J Plast* 26:1527–1540
11. Narayanan KR, Subbiah S, Sridhar I (2011) Indentation response of single-crystal copper using rate-independent crystal plasticity. *Appl Phys A* 105:453–461
12. Eidel B (2011) Crystal plasticity finite-element analysis versus experimental results of pyramidal indentation into (001) fcc single crystal. *Acta Mater* 59:1761–1771
13. Dyer LD (1965) The actual dislocation distribution around a ball indentation on the cube face of copper. *Trans ASM* 58:620–643
14. Hollatz M, Bobeth M, Pompe W, Marx V (1996) Orientation dependent crack patterns in alumina films on NiAl single crystals due to spherical indentation. *Acta Mater* 44:4149–4159
15. Stelmashenko NA, Walls MG, Brown LM, Milman YV (1993) Microindentations on W and Mo oriented single crystals: an STM study. *Acta Metall Mater* 41:2855–2865
16. Lim YY, Bushby AJ, Chaudhri MM (1998) Nano and macro indentation studies of polycrystalline copper using spherical indenters. *Mater Res Soc Symp Proc* 522:145–150
17. Lim YY, Chaudhri MM (2002) The influence of grain size on the indentation hardness of high-purity copper and aluminum. *Philos Mag A* 82:2071–2080
18. Wo PC, Ngan AHW, Chiu YL (2006) TEM measurement of nano-indentation plastic zones in Ni₃Al. *Scripta Mater* 55:557–560
19. Wo PC, Ngan AHW (2004) Investigation of slip transmission behavior across grain boundaries in polycrystalline Ni₃Al using nanoindentation. *J Mater Res* 19(01):189–201
20. Sansoz F (2011) Atomistic processes controlling flow stress scaling during compression of nanoscale face-centered-cubic. *Acta Mater* 59:3364–3372
21. Salehinia I, Bahr DF (2014) Crystal orientation effect on dislocation nucleation and multiplication in FCC single crystal under uniaxial loading. *Int J Plast* 52:133–146
22. Miller RE, Rodney D (2008) On the nonlocal nature of dislocation nucleation during nanoindentation. *J Mech Phys Solids* 56:1203–1223
23. Hill R, Rice JR (1972) Constitutive analysis of elastic–plastic crystals at arbitrary strain. *J Mech Phys Solids* 20:401–413
24. Asaro RJ (1983) Micromechanics of crystals and polycrystals. *Adv Appl Mech* 23:1–115
25. Gambin W (1992) Refined analysis of elastic–plastic crystals. *Int J Solids Struct* 29:2013–2021
26. Tome C, Canova GR, Kocks UF, Christodoulou N, Jonas JJ (1984) The relation between macroscopic and microscopic strain hardening in f.c.c. polycrystals. *Acta Metall* 32:1637–1653
27. Miehe C (1996) Exponential map algorithm for stress updates in anisotropic multiplicative elastoplasticity for single crystals. *Int J Numer Methods Eng* 39:3367–3390
28. de Souza Neto EA, Peric D, Dutko M, Owen DRJ (1996) Design of simple low order finite elements for large strain analysis of nearly incompressible solids. *Int J Solids Struct* 33:3277–3296
29. Alart P, Cumier A (1991) A mixed formulation for frictional contact problems prone to Newton like solution methods. *Comput Methods Appl Mech Eng* 92:353–375
30. Korelc J (2009) Automation of primal and sensitivity analysis of transient coupled problems. *Comput Mech* 44:631–649
31. Lengiewicz J, Korelc J, Stupkiewicz S (2011) Automation of finite element formulations for large deformation contact problems. *Int J Numer Methods Eng* 85:1252–1279
32. Ortiz M, Repetto EA, Stainier L (2000) A theory of subgrain dislocation structures. *J Mech Phys Solids* 48:2077–2114
33. Petryk H, Kurka M (2013) The energy criterion for deformation banding in ductile single crystals. *J Mech Phys Solids* 61:1854–1875